ACS APPLIED MATERIALS & INTERFACES

www.acsami.org

Research Article

# Magnetically Assembled Ultrablack Surface with Omnidirectional and Broadband Light Absorption

Huiyong Li,† Chen Shen,† Shuai Sun, Chun Li,* Hui Zhang,* and Zhong Zhang*

Cite This: *ACS Appl. Mater. Interfaces* 2023, 15, 11369−11378

Read Online

ACCESS | Metrics & More | Article Recommendations | Supporting Information

**ABSTRACT:** Ultrablack surfaces with stable and omnidirectional light absorption over a wide spectral range are fundamentally crucial for applications concerning strict optical requirements from high-end optical to solar−heat conversion devices. Inspired by nature, we report a needle-like array structure (NAS) prepared by spraying and self-assembling the magnetic composite ink under an external magnetic field. With high structure regularity and small feature size, the NAS presents extremely low hemispherical reflectance (≤0.3%) over a wide spectral range of 300−2000 nm and stable omnidirectional absorption (incident angle insensitivity up to 70°), which could be one of the darkest surfaces ever reported. The exciting light absorption performance can be attributed to the synergistic effects of (1) structural absorption caused by multiple scattering between array units and (2) strong forward scattering and high light absorptivity of magnetic particles. The NAS exhibits outstanding photothermal conversion for solar harvesting, self-cleaning performance, good flexibility, and thermal-aging resistance, offering an appealing alternative to construct ultrablack surfaces for practical applications.

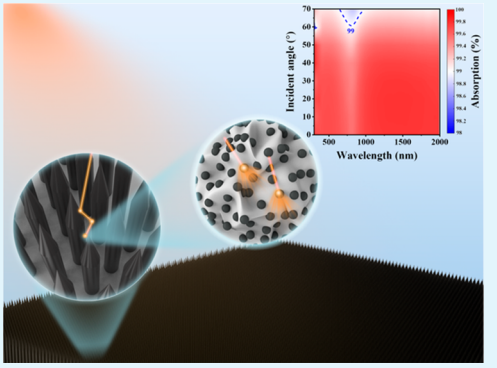


**KEYWORDS:** *ultrablack surface, array structure, structural absorption, omnidirectional absorption, magnetically driven self-assembly*



## 1. INTRODUCTION

Ultrablack materials, featured with low surface reflectance and excellent light absorption performance, play an essential role in high-performance optical devices,[1,2] solar energy harvesting,[3−5] and infrared stealth.[6,7] Theoretically, an ideal ultrablack material should absorb almost total incident light waves over a broadband wavelength range, regardless of incident angles. A moth-eye structure, featured with unique subwavelength-sized corneal nipple arrays,[8] is the classic structure imitated for guiding the preparation of ultrablack surfaces. According to Fresnel's law, reflection inevitably occurs at the air−matrix interface because of the discontinuity of the refractive index.[9−12] However, subwavelength nipples on moth eyes create a gradient refractive index change at the interface, effectively suppressing surface reflection. Over the past few decades, several methods have been proposed to mimic this distinctive nanoarray structure for improving light absorption performance. For example, chemical vapor deposition (CVD) is often used to prepare carbon nanotube arrays with unique optical properties;[13,14] the single-walled carbon nanotube (SWNT) forest prepared exhibited low reflectance (<1%) over a wide spectral range (0.2−200 μm).[15] Chemical etching is another effective way to construct nanosized array structures.[16−19] After etching, a nanostructured array appeared on the silicon surface, significantly enhancing light absorption. Despite giving elaborate structures, the strategies mentioned above have inherent limitations on preparation conditions and manufacturing scalability. Therefore, a simple and inexpensive preparation method of the array structure with highly effective light absorption is urgently needed in practice.

Recently, feathers of birds-of-paradise[20] and peacock spiders[21] have been revealed and studied for superblack appearances. Their feature size is on the microscale (e.g., modified barbule arrays for birds-of-paradise and highly packed microlens arrays for peacock spiders), relatively larger than the nanosized structure of the moth eye. The dominant light absorption mechanism is the multiple light reflection/scattering and absorption rather than the light interference in the nanoarray. As incident light travels to the microarray, most of it will enter the deep cavities between array units, where multiple light reflection/absorption occurs. In addition, microarray structures have advantages in preparation and mechanical robustness over the nanosized structures, which are vital to real applications.

In this article, we prepared microarray ultrablack surfaces via a magnetically driven self-assembly method. During spraying, polydimethylsiloxane (PDMS)@$Fe_3O_4$ droplets can sponta-

Received: December 20, 2022
Accepted: February 7, 2023
Published: February 17, 2023

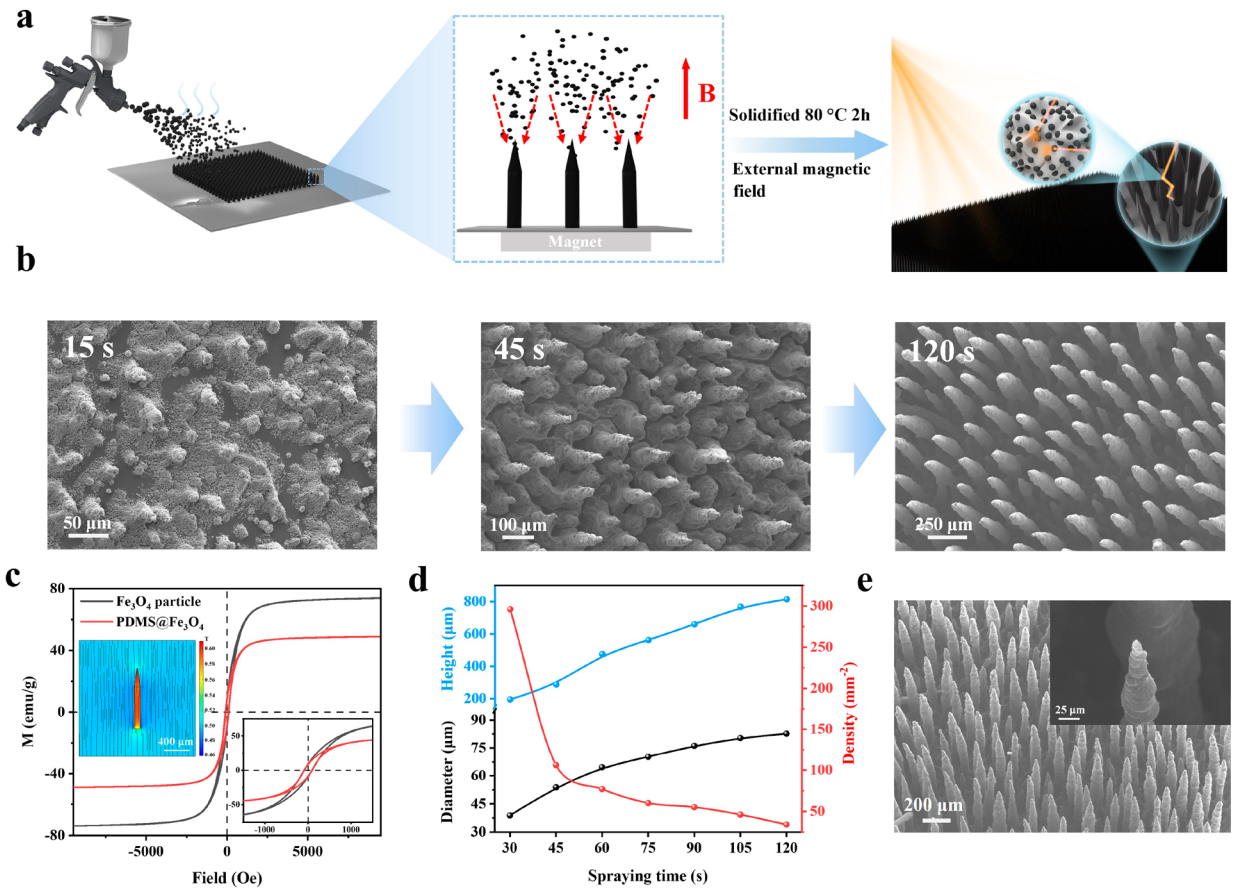


**Figure 1.** Preparation process and morphology of NAS. (a) Schematic illustration of the preparation of NAS via the spraying technique and magnetic field. (b) SEM morphology evolution of NAS during the spraying process at three typical stages. (c) *M*−*H* hysteresis loops for pure $Fe_3O_4$ particles and PDMS@$Fe_3O_4$ composite. The left inset is the simulated magnetic field distribution in a single needle under an external magnetic field of 500 mT, and the right inset is the enlarged magnetic hysteresis loops. (d) Average height, diameter, and density of needles during the spraying process under an external magnetic field of 500 mT. (e) Top view SEM with a 5° tilt angle of NAS prepared under 500 mT with a spraying time of 120 s. The inset is the SEM closeup for the cone tip.

neously form a vertically aligned needle-like array structure (NAS), which can be facilely tuned by an external magnetic field strength and spraying time. The NAS consisting of the cone tip and cylinder below has unique structural advantages for light collecting and dissipation: the sharp cone tips significantly reduce surface reflection and allow most light to enter the array, while the cylinders form deep array cavities, which cause multiple light scattering, extending the light propagation path and improving light absorption. The resulting ultrablack surfaces exhibited extremely low light reflectance (lowest value of 0.3%), omnidirectional light absorption, as well as good comprehensive performance.

## 2. RESULTS AND DISCUSSION

The NAS was prepared by spraying magnetic PDMS@$Fe_3O_4$ composite ink under an external magnetic field, as schematically illustrated in Figure 1a. The PDMS@$Fe_3O_4$ composite ink was homogeneously dissolved in petroleum ether and then sprayed out under airflow. The solvent evaporated during the spraying process, leaving PDMS-encapsulated $Fe_3O_4$ droplets to self-assemble on the substrate. Figure 1b and Figure S1 of the Supporting Information demonstrate the structure morphology evolution during preparation, which could be divided into three typical stages. Composite droplets were deposited randomly on the substrate at the early stage (15 and 30 s), forming irregular protrusions. With spraying continuing, adjacent protrusions aggregated together, giving tiny cone-like structures. Finally, under the external magnetic field, tiny cone-like structures constantly attracted sprayed droplets to deposit on their tops, forming NAS with a high aspect ratio and good verticality.

The magnetic response of the PDMS@$Fe_3O_4$ composite under an external magnetic field induces the self-assembly growth of NAS on the substrate. Figure 1c shows the magnetic hysteresis loops of $Fe_3O_4$ nanoparticles and the PDMS@$Fe_3O_4$ composite. Misaligned hysteresis loops were obtained for both materials (Figure 1c), implying that both are ferromagnetic.[22] As a result of the ferromagnetism, deposited PDMS@$Fe_3O_4$ during spraying is magnetized under the external magnetic field.[23] The relative permeability of PDMS@$Fe_3O_4$ is 1.21, which means that the induced magnetic field strength in the deposited needle-like structure is higher than that of the background, as simulated in Figure 1c and Figure S2 of the Supporting Information. For structures under different spraying times, there is always a gradient change in the induced magnetic field strength along the structure, which reaches the highest value around the needle tip. Sprayed composite droplets would be attracted to the needle tip, causing a continuous increase in the structure height (Figure 1d and Figure S3 of the Supporting Information). Because of


https://doi.org/10.1021/acsami.2c19796
ACS Appl. Mater. Interfaces 2023, 15, 11369−11378

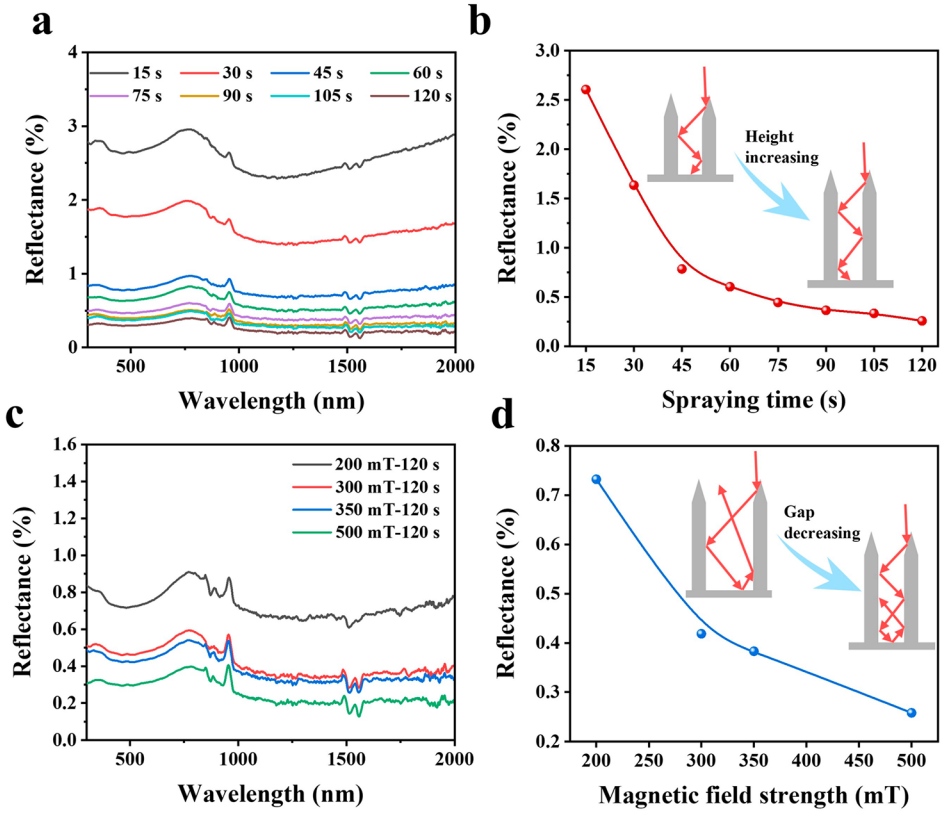


**Figure 2.** Light reflectance performance of NAS. (a) Hemispherical reflectance spectra for NAS prepared under 500 mT with different spraying times. (b) Average $R_s$ values as a function of the spraying time. (c) Hemispherical reflectance spectra for NAS prepared under different magnetic field strengths with the same spraying time of 120 s. (d) Average $R_s$ values as a function of the magnetic field strength.

the dynamic balance of surface tension, magnetic force, and gravity,[24] cylindricality is always obtained at the bottom, while the diameter contracts at the top, forming a cone tip. With spraying continuing, the average height and diameter of the needle structure gradually increase, while the density decreases synchronously (Figure 1d and Figure S3 of the Supporting Information).

The composite films have unique needle-like structures, which greatly benefit the trapping and dissipation of incident light waves. The simulated ray-tracing result, shown in Figure S4 of the Supporting Information, compares the simulated reflectance of array structures made up of three different shaped array units (microsized cylinder, cone, and needle arrays). Here, the array units are set to have the same nominal diameter and height but different unit gaps (i.e., different unit densities). It is found that the cylinder array holds high light reflectance because of its rather huge plane surface on the cylinder top, where the reflected light leaves and propagates outward and cannot be absorbed by the array (inset I in Figure S4b of the Supporting Information). For the cone array, as a result of its specific structure (wide space at the top but narrow space at the bottom), there is a certain chance for the light reflected from the bottom to escape without encountering the neighboring cone unit[25] (inset II in Figure S4b of the Supporting Information); therefore, the reflectance is sensitive to the unit gap. Comparatively, the needle array consisting of a sharp cone tip at the top and cylinder below may have unique advantages over the above two arrays. On the one hand, the high-resolution cone tips significantly decrease the filling ratio of the composite material, leading to a gradient change of refractive index from air to film, bringing a better impedance match, and suppressing surface light reflection significantly. On the other hand, the light entering the cavities is trapped by the cylinder array and reflected/scattered repeatedly until completely absorbed (inset III in Figure S4b of the Supporting Information).

Figure 2 reveals the influence of processing parameters (spraying time and magnetic field strength) of the NAS on the light reflection performance. Panels a and b of Figure 2 show the hemispherical reflectance spectra and related average reflectance ($R_s$) of samples prepared at different spraying times under an external magnetic field of 500 mT. $R_s$ decreases significantly with increasing the spraying time. Note that the height, diameter, and density of NAS change simultaneously with increasing the spraying time (Figure 1d and Figure S3 of the Supporting Information), clarifying that the contribution of each unit feature seems difficult. In general, at a shorter spraying time, there are many randomly arranged protrusions (panels b–e of Figure S4 of the Supporting Information) and the height for the array unit is too short that there is not a deep enough cavity to trap incident light; therefore, a high $R_s$ value remains. As the spraying time continues, the array height and diameter increase rapidly, forming deep cavities (panels f–i of Figure S4 of the Supporting Information) and, thus, greatly enhancing the light-trapping ability. When the array height exceeds 500 $\mu$m, the $R_s$ value decreases slowly and remains stable under 0.5%.

The magnetic field strength, like the spraying time, has a similar effect on sample reflectance (panels c and d of Figure 2 and Figure S5 of the Supporting Information). Typically, panels c and d of Figure 2 present the hemispherical reflectance spectra and related average reflectance of samples


https://doi.org/10.1021/acsami.2c19796
ACS Appl. Mater. Interfaces 2023, 15, 11369–11378

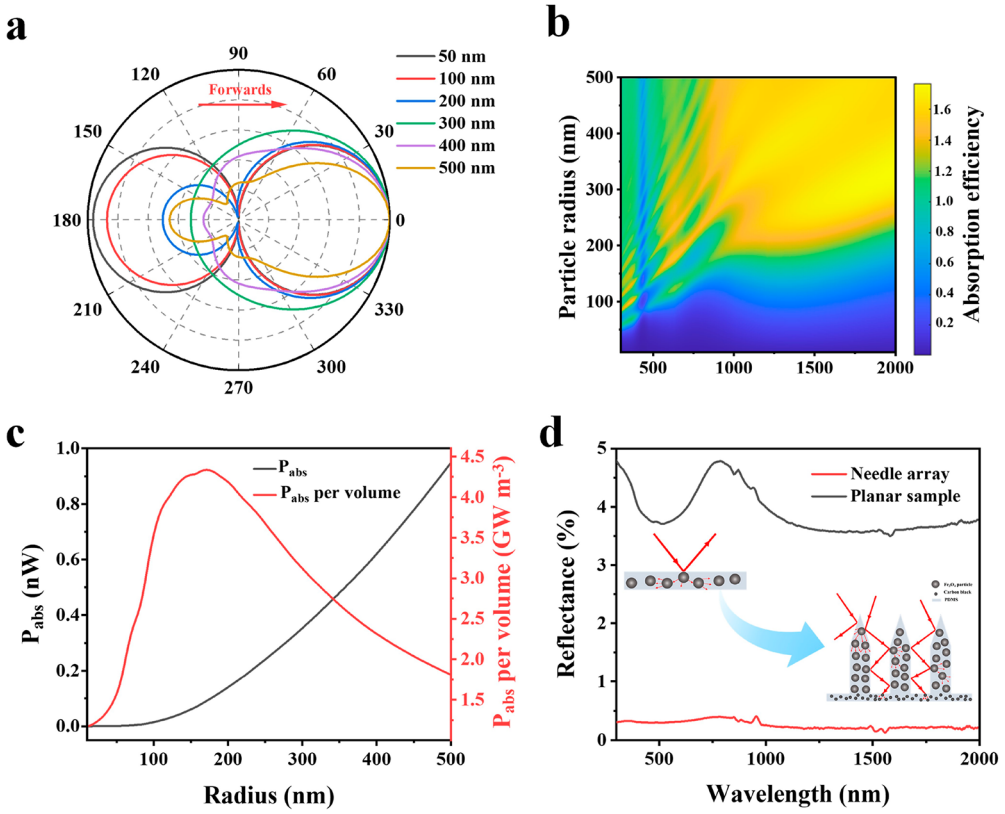


**Figure 3.** (a) Scattering phase functions for $Fe_3O_4$ particles at $\lambda$ = 500 nm with different diameters, where 0° represents the direction of incident light. (b) Simulation of the normalized absorption efficiency of $Fe_3O_4$ particles over the wavelength range of 300−2000 nm with the particle radius varying from 10 to 500 nm. (c) Absorption power and absorption power per volume of $Fe_3O_4$ particles as a function of the particle radius in solar radiation spectra. (d) Light reflectance comparison between the NAS and planar sample.

prepared under different magnetic field strengths with the same spraying time of 120 s. $R_s$ of samples decreases significantly with the magnetic field strength. This may probably be due to the decreased unit gap (i.e., increased unit density) with the increased magnetic field strength (Figure S5 of the Supporting Information), which favors the construction of high-quality light microtraps, where light can be reflected and/or scattered repeatedly until absorbed.

Apart from the unique structure, the material component plays an essential role in the light absorption performance. The scanning electron microscopy (SEM) image of a single broken needle (Figure S8 of the Supporting Information) suggests that the needle is actually composed of a thin, neat PDMS skin and PDMS@$Fe_3O_4$ composite core. The formation of this specific structure is likely due to the fact that the magnetic $Fe_3O_4$ nanoparticles aggregate into a chain under an external magnetic field; therefore, some redundant PDMS resin is squeezed from the core. Figure S9 of the Supporting Information presents the experimental complex spectral refractive index of PDMS and $Fe_3O_4$ in the wavelength of 300−2000 nm. The $n$ value for PDMS (constant, ∼1.4) is lower than that of $Fe_3O_4$ (2.1−2.5); therefore, it is reasonable to consider that the refractive index may gradiently change from the skin to the core, benefiting the refractive index match with air and, thus, minimizing the interfacial reflection. Moreover, PDMS maintains an extremely low $\kappa$ value (nearly 0) over the whole wavelength range, with most incident light just penetrating it[26] and then being absorbed by $Fe_3O_4$ with a relatively high $\kappa$ value.

According to the particle size ratio to light wavelength, three predominantly scattering mechanisms can be defined:[27] Rayleigh scattering, Mie scattering, and geometric scattering. Because the particle size is comparable to the light wavelength, Mie scattering dominates the scattering behavior. With reference to the Mie scattering theory, two parameters, i.e., the scattering phase function of particles and the absorption efficiency, are crucial for improving light absorption. The scattering phase function describes the directional dependence of scattered light, while the absorption efficiency is defined as the energy ratio of absorbed light to the incident light.[28] It is known that the particles, which show strong forward scattering and high absorption efficiency, are beneficial for light absorption. Herein, COMSOL Multiphysics software was used to explore the scattering phase functions for $Fe_3O_4$ particles of various sizes. The simulation method is described in Figure S10 of the Supporting Information. Figure 3a depicts that Rayleigh scattering occurs at a small particle size (diameter of ≤100 nm), resulting in a nearly symmetrical pattern for the scattering phase function; when the particle diameter is >100 nm, the scattering behavior lies in the Mie scattering region, where the forward scattering phase function dominates. Figure 3b shows the absorption efficiency of $Fe_3O_4$ particles of various sizes. In the near-infrared (NIR) wavelength (1000−2000 nm), the absorption efficiency of $Fe_3O_4$ particles increases gradually with the particle radius increasing and remains at a high value when the radius exceeds 200 nm. Comparatively, the absorption efficiency in the visible (vis)−NIR wavelength (300−1000 nm) is smaller than that in 1000−2000 nm.



https://doi.org/10.1021/acsami.2c19796
ACS Appl. Mater. Interfaces 2023, 15, 11369−11378

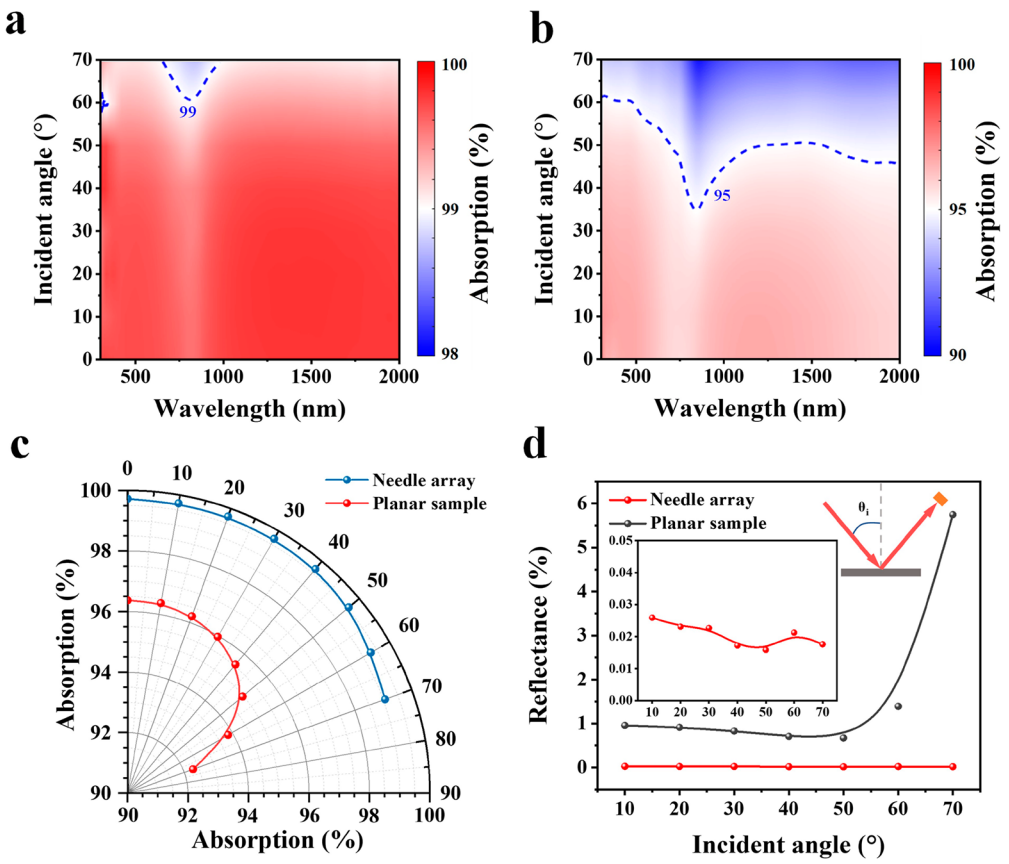


**Figure 4.** Comparison of incident angle dependence of light absorption between the NAS and planar sample. (a and b) Experimental light absorption spectra. (c) Average hemispherical absorption as a function of the incident angle. (d) Average specular reflectance. The inset is the enlarged local curve for NAS.

**Table 1. Comparison of the Light Reflectance and Preparation Conditions of Some Reported Ultrablack Surfaces**

| material | lowest reflectance (%) | test wavelength | preparation technique and processing conditions | reference |
|---|---|---|---|---|
| vertically aligned single-walled carbon nanotubes | 1 | 0.2−200 $\mu$m | CVD, on the Si substrate at 750 °C | 15 |
| vertically aligned multi-walled carbon nanotubes | 0.1 | 0.4−4 $\mu$m | CVD, on the Si/$LiTaO_3$ substrate at 750 °C | 33 |
| | 1 | 4−14 $\mu$m | | |
| vertically aligned carbon nanotube forests | <0.5 | 400−800 nm | CVD, on the Si substrate at 500−800 °C | 34 |
| vertically aligned carbon nanotube array | <1 | 2.5−15 $\mu$m | photothermal chemical vapor deposition (PTCVD), on the Al substrate at 425 °C | 2 |
| vertically aligned carbon nanotube array | 0.045 | 457−633 nm | CVD | 35 |
| carbon-fiber piles | 0.51 | 0.2−2.5 $\mu$m | electrostatic flocking | 36 |
| nanostructured silicon | 1.3 | 400−1100 nm | self-assembled nanosphere lithography | 37 |
| microstructured aluminum-doped silicon films | 0.7 | 350−2000 nm | (1) co-sputtering Si and Al on the Si substrate; (2) NaOH etching | 19 |
| subwavelength-structured silicon surface | 0.5 | 0.2−2.5 $\mu$m | fast atom beam (FAB) etching | 38 |
| silicon nanotip arrays | <1 | 0.2−2.4 $\mu$m | electron cyclotron resonance (ECR) plasma etching | 18 |
| silicon nanowire arrays | 0.8 | 300−1200 nm | laser interference lithography and metal-assisted chemical etching | 17 |
| nanostructure-covered conical microstructures (NC-CMs) on Ni | <3 | 0.25−1 $\mu$m | femtosecond laser irradiation | 39 |
| microspike on the stainless-steel surface | 4.9 | 350−1750 nm | ultrashort pulse laser (UPL) texturing | 40 |
| micro/nanoconical pillar structures on metal surfaces | 1.8 | 405−1550 nm | ultrafast laser processing | 41 |
| black Au film | 8 | 300−600 nm | physical vapor deposition (PVD) | 42 |
| self-assembly gold nanoparticles | <1 | 0.4−10 $\mu$m | PVD | 3 |
| 3D silica scaffold and Ag nanoparticles | 2 | 250−2500 nm | hybird PVD and atomic layer deposition (ALD) | 43 |
| microconvex-structured PDMS@PANI composite film | 0.7 | 400−800 nm | template casting | 26 |
| PDMS@$Fe_3O_4$ needle array | 0.3 | 300−2000 nm | magnetically assembly and spraying process | this work |



https://doi.org/10.1021/acsami.2c19796
ACS Appl. Mater. Interfaces 2023, 15, 11369−11378

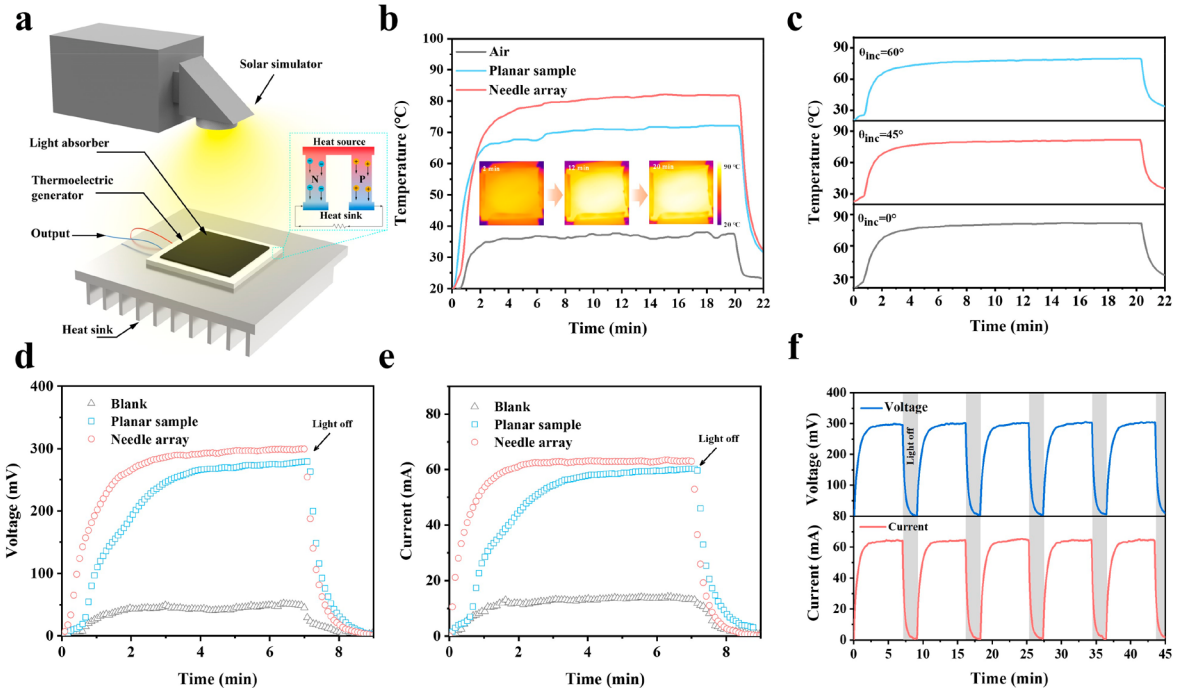


**Figure 5.** (a) Schematic illustration of the STEG prototype. (b) Temperature−time curves of different samples illuminated under solar power of 1.5 kW $m^{-2}$. The insets are infrared (IR) images of NAS at different illumination times. (c) Temperature−time curves of NAS under different solar light incident angles. (d) $V_{oc}$ and (e) $I_{sc}$ yielded from STEG prototypes upon illumination. (f) Cycling stability of $V_{oc}$ and $I_{sc}$ for the NAS-based STEG prototype.

To clearly illustrate the light absorption ability of particles in a certain wavelength, we calculated the absorption power ($P_{abs}$) and the absorption power per unit volume (refer to eqs 2 and 3 in section 4.3 and Figure 3c). In this work, the wavelength is the solar radiation spectra (Figure S11 of the Supporting Information), where more than half of the power distributes in 300−1000 nm.[28,29] Figure 3c presents $P_{abs}$ increasing monotonically as the particle radius increases, while $P_{abs}$ per unit volume reaches its highest value with the particle radius at around 150 nm (i.e., diameter = 300 nm). This particle diameter approximates the mean diameter of $Fe_3O_4$ particles employed here (~220 nm; Figure S12 of the Supporting Information), verifying their excellent solar light absorption performance.

As a summary, benefiting from the unique needle array structure, proper particle size, as well as excellent solar light absorption of particles, the light absorption mechanism can be concluded as follows: When incident light reaches the surface of a single needle unit, because PDMS is highly transparent, most light would penetrate and further be scattered and absorbed by $Fe_3O_4$ particles. Strong forward scattering and high light absorptivity ensure the complete absorption of entering light. On the other hand, the reflected light at the surface would further propagate and be absorbed by adjacent needle units. With reflection−absorption between the needle array repeating, a low reflectance can be realized eventually (Figure 3d).

In practical terms, ultrablack surfaces are expected to exhibit stable omnidirectional absorption, regardless of the incident angle, which calls for strict requirements for the material and structure. We further experimentally measured the angle dependence of the light absorption performance of the NAS and planar sample from 0° to 70° in the broad spectral region from 300 to 2000 nm using ultraviolet (UV)−vis−NIR spectroscopy with an integrating sphere. As shown in Figure 4a, the hemispherical absorption for NAS remains unprecedentedly stable under various angles of incidence (AOIs), in stark contrast with the significant change in light absorption with AOI for the planar sample (Figure 4b); the absorption still reaches 98% over the whole wavelength, even when the incident angle is up to 60° (Figure 4a). Figure 4c presents that the average absorption value for the NAS is ~99% in the incident angle range of 0−70°. To clearly illustrate the reflection characteristics of NAS, we conducted a specular reflectance measurement on the NAS and planar sample under various incident angles. It is vividly shown in Figure 4d that NAS has a low specular reflectance (<0.03%) under all incident angles, reducing by 2 orders of magnitude compared to that of the planar sample. The specular reflectance of NAS accounts for less than a tenth of total reflectance, implying the diffusive reflectance feature for NAS.[10] As discussed before, the tiny cone tips (~5 μm) of NAS are able to redirect light off the normal reflection direction,[21] and the diffused light will be reflected and absorbed repeatedly between the neatly arranged needles, resulting in stable omnidirectional light absorption. Table 1 compares the light reflectance performance of different ultrablack surfaces in the literature, and our material is one of the darkest surfaces ever reported. Note that, even though some carbon nanotube (CNT) arrays show slightly lower reflectance than NAS, they usually need much higher temperatures, special atmospheres, and high-temperature-resistant substrates to fabricate, still limiting their large-scale practice thus far. On the contrary, the processing conditions for NAS are relatively mild and low-cost, suitable for more applications.

As revealed above, the NAS has low reflectance and high absorbance over 300−2000 nm (UV, vis, and NIR). This outstanding absorbance may be used for solar−thermal−


https://doi.org/10.1021/acsami.2c19796
ACS Appl. Mater. Interfaces 2023, 15, 11369−11378

electric generation (STEG) applications. We demonstrate a STEG prototype based on the solar−thermal transition effect of the light absorber. As illuminated in Figure 5a, the light absorber (made of NAS or planar black coating) is finely attached to a commercial TEG device, of which the bottom is coupled with a heat sink. Under the solar simulator illumination, the temperature difference of the TEG sides results in an open circuit voltage ($V_{oc}$) and short circuit current ($I_{sc}$) between them as a result of the Seebeck effect. The higher the temperature difference, the larger $V_{oc}$ and $I_{sc}$.

Figure 5b displays that NAS shows a rapid temperature increase under the first 2 min of illumination and reaches the equilibrium temperature in 6 min of illumination; the equilibrium temperature of NAS is ∼10 °C higher than that of the planar black sample, owing to the higher light absorbance of NAS. Furthermore, the temperature-increasing curves change slightly under various light incident angles (Figure 5c), reflecting the outstanding omnidirectional performance of NAS. With the solar illumination time increasing, the temperature difference between the two sides of the TEG device increases, finally generating steady electric output. The maximum $V_{oc}$ and $I_{sc}$ of NAS-based STEG are higher than those of the planar black sample and even 6 times higher than that of the blank TEG device (panels d and e of Figure 5). More importantly, NAS-based STEG can repeatedly respond to the light on−off cycle without any change (Figure 5f).

On top of that, owing to its large aspect ratio and high tip resolution, the NAS film exhibits excellent hydrophobic performance. Because PDMS is intrinsically hydrophobic, the planar structure film exhibits hydrophobicity (Figure S14 of the Supporting Information); however, the high aspect ratio array structure further enhanced the hydrophobicity combined with a smaller rolling angle. PDMS itself is a typical flexible polymer;[30] therefore, NAS made up of the PDMS@$Fe_3O_4$ composite holds good elasticity, as shown in Figure S15 of the Supporting Information. The film shows no appreciable damage after being bent 100 times, and its light absorption performance remains unchanged. Moreover, after aging under the ambient air at 150 °C for 4 weeks, there is only a slight decrease in the light absorption performance, which may result from the oxidation of $Fe_3O_4$ particles. However, the PDMS matrix slows the oxidation rate,[31,32] endowing it with stable light absorption performance under a high temperature. Overall, these wonderful features make NAS adaptable to various working conditions.

## 3. CONCLUSION

In summary, we successfully prepared a NAS through a magnetically driven self-assembly and spraying technique. With high structural regularity and small feature size, the NAS exhibits extremely low hemispherical reflectance (≤0.3%) over a wide spectral range of 300−2000 nm and stable omnidirectional absorption, even at the incident angle as high as 70°, outperforming the most ultrablack surfaces ever reported. The ultrablackness is attributed to the multiple scattering/absorption between needle array units and the high absorption/strong forward scattering ability of the magnetic nanoparticles. This work demonstrates that the NAS was valuable for wide-angle solar energy harvesting and photothermal convection, benefiting the solar−thermal−electric effect in the assembled STEG system. Meanwhile, the NAS was superhydrophobic, flexible, and thermal-aging-resistant, highlighting its application in various working conditions.

## 4. EXPERIMENTAL SECTION

**4.1. Materials.** PDMS (SYLGARD 184) was purchased from Dow Corning Organic Silicon Co., Ltd. (Beijing, China). $Fe_3O_4$ was supplied by Maclin Bio-Chem Technology Co., Ltd. (Shanghai, China). Its SEM image and size distribution are shown in Figure S12 of the Supporting Information. Petroleum ether was obtained from Modern Oriental Technology Development Co., Ltd. (Beijing, China). Carbon black (CB) FW200 was purchased from Evonik Industries AG (Germany). All agents were used as received without further purification.

**4.2. Preparation of $Fe_3O_4$@PDMS NAS.** The preparation of $Fe_3O_4$@PDMS light absorbers involves two main steps. (1) Precoating the substrate: First, a thin PDMS@CB with the CB mass fraction at 3% was sprayed on an aluminum foil (cut into 5 × 5 cm). After spraying, pretreated substrates were put in an oven under 80 °C for 2 h for subsequent use. (2) Establishing magnetically driven self-assembly of $Fe_3O_4$@PDMS ink under spraying: First, 2.5 g of $Fe_3O_4$, 2.5 g of PDMS, and 15 g of petroleum ether were fully mixed under 2000 rpm rotation for 5 min. Then, the obtained ink was sprayed on the pretreated substrate under an external magnetic field. Four permanent magnets with center surface magnetism at 250, 300, 350, and 500 mT were employed to generate the magnetic field. The spraying process lasts for 15−120 s, with an interval of 15 s. The spray gun caliber and pressure were set at 0.3 mm and 0.2 MPa, respectively. After spraying, the prepared $Fe_3O_4$@PDMS composite film was solidified under 80 °C for 2 h with the presence of the external magnetic field.

**4.3. Characterization.** The morphology of samples and size distribution of $Fe_3O_4$ nanoparticles were observed by field-emission scanning electron microscopy (Hitachi SU 8010, Japan). Before observation, the samples were cut after being soaked in liquid nitrogen and sputtered with thin platinum. The height of array structures was observed by an optical microscope (DM4000, Leica Industries, Buffalo Grove, IL, U.S.A.). The magnetic hysteresis loops of the $Fe_3O_4$ nanoparticle and $Fe_3O_4$@PDMS were measured by a vibrating sample magnetometer (VSM, Lake Shore 8604, Westerville, OH, U.S.A.). Water contact angles were measured on a contact angle system (DSA100, Krüss, Germany). Reflectance spectra in the IR band (2.5−20 $\mu$m) was measured by the Fourier transform infrared spectrometer (Vertex 80v, Bruker, Germany, equipped with a gold integrating sphere and gold-coated Al foil as the reference).

The UV−vis−NIR absorbance spectrum was measured by a Lambda 950 spectrophotometer (PerkinElmer, Waltham, MA, U.S.A.) with an integrating sphere collecting reflected light. A $BaSO_4$ white diffuser was employed for the calibration before test, and the wavelength range and scanning speed were set at 300−2000 nm and 2 nm/s, respectively. With reference to normal hemispherical reflectance spectra, samples were attached to the end of the beam path. For the omnidirectional reflectance measurement, a clip-style sample holder that hung inside the integrating sphere was employed to change the incident angle accordingly (Figure S6 of the Supporting Information). As samples were prepared on the Al substrate, there is no transmittance ($T_s = 0$); therefore, the absorbance can be calculated as

$$A_s = 1 - R_s \tag{1}$$

where $R_s$ is the absorbance defined as the power ratio of reflected light to incident light.

The absorption power of $Fe_3O_4$ particles can be calculated as[44]

$$C_{abs}(\lambda) = Q_{abs}\pi r^2 \tag{2}$$

$$P_{abs} = \int_{\lambda_{min}}^{\lambda_{max}} I(\lambda)C_{abs}(\lambda)\mathrm{d}\lambda \tag{3}$$

where $Q_{abs}$ is the absorption efficiency calculated from Mie scattering, $r$ is the particle radius, $I(\lambda)$ is the intensity of solar radiation (AM 1.5



https://doi.org/10.1021/acsami.2c19796
ACS Appl. Mater. Interfaces 2023, 15, 11369−11378

G), $C_{abs}(\lambda)$ is the absorption cross section, and $\lambda_{max}$ and $\lambda_{min}$ correspond to the solar radiation spectral range calculated, which is 300−2000 nm in this article.

COMSOL Multiphysics (version 5.6, COMSOL, Inc., Sweden) was used to simulate the magnetic field distributions of permanent magnets and along the array structures.

The solar−thermal−electrical conversion test was conducted on the basis of a commercial thermoelectric generator (TEG-127220, 4 × 4 cm). The bottom of the TEG devices was attached to a heat sink immersed in ice water, and our light absorber was attached to the top of the TEG device. A computer-controlled digital source meter recorded the generated voltage and current (Keithley DMM7510). Solar illumination was conducted by the solar simulator (Solar MH 2500, Numi, China), and the IR images of samples were taken by a portable thermal imaging camera (TiX560 IR camera, Fluke, Everett, WA, U.S.A.).

## ■ ASSOCIATED CONTENT

### Supporting Information

The Supporting Information is available free of charge at https://pubs.acs.org/doi/10.1021/acsami.2c19796.

SEM images of morphology evolution for NAS (Figure S1), simulated magnetic field distribution during spraying and needle height changes for NAS (Figure S2), statistical results of morphology parameters for NAS at various spraying times under different magnetic field strengths (Figure S3), ray tracing simulation result for three different array units (Figure S4), tilted top-view SEM image comparison for NAS (Figure S5), schematic illustration of the measurement of hemispherical reflectance and omnidirectional reflectance (Figure S6), hemispherical reflectance for NAS (Figure S7), SEM image of a single needle (Figure S8), experimental complex refractive index for PDMS and $Fe_3O_4$ and reflectance, transmittance, and absorbance of the pure PDMS film (Figure S9), Mie scattering simulation schematic illustration (Figure S10), solar irradiation spectra (Figure S11), SEM image and particle size distribution for the $Fe_3O_4$ particle (Figure S12), hemispherical reflection spectra at the NIR−MIR band (Figure S13), contact and rolling angles for NAS and planar sample (Figure S14), and bending and aging test of NAS (Figure S15) (PDF)

Rolling angle of the NAS (Movie 1), contact angle of the NAS (Movie 2), and rolling angle of the planar sample (Movie 3) (MP4)

## ■ AUTHOR INFORMATION


### Corresponding Authors

**Chun Li** − *Key Lab of Organic Optoelectronics and Molecular Engineering of Ministry of Education, Laboratory of Flexible Electronics Technology, Department of Chemistry, Tsinghua University, Beijing 100084, People's Republic of China;* orcid.org/0000-0002-3132-3756; Email: chunli@mail.tsinghua.edu.cn

**Hui Zhang** − *CAS Key Laboratory of Nanosystem and Hierarchical Fabrication, CAS Center for Excellence in Nanoscience, National Center for Nanoscience and Technology, Beijing 100190, People's Republic of China;* orcid.org/0000-0002-5202-1175; Email: zhangh@nanoctr.cn

**Zhong Zhang** − *CAS Key Laboratory of Mechanical Behavior and Design of Materials, Department of Modern Mechanics, University of Science and Technology of China, Hefei, Anhui 230027, People's Republic of China;* orcid.org/0000-0002-9102-1311; Email: zhongzhang@ustc.edu.cn

### Authors

**Huiyong Li** − *CAS Key Laboratory of Nanosystem and Hierarchical Fabrication, CAS Center for Excellence in Nanoscience, National Center for Nanoscience and Technology, Beijing 100190, People's Republic of China; Key Lab of Organic Optoelectronics and Molecular Engineering of Ministry of Education, Laboratory of Flexible Electronics Technology, Department of Chemistry, Tsinghua University, Beijing 100084, People's Republic of China*

**Chen Shen** − *CAS Key Laboratory of Nanosystem and Hierarchical Fabrication, CAS Center for Excellence in Nanoscience, National Center for Nanoscience and Technology, Beijing 100190, People's Republic of China; University of Chinese Academy of Sciences, Beijing 100049, People's Republic of China*

**Shuai Sun** − *CAS Key Laboratory of Nanosystem and Hierarchical Fabrication, CAS Center for Excellence in Nanoscience, National Center for Nanoscience and Technology, Beijing 100190, People's Republic of China; University of Chinese Academy of Sciences, Beijing 100049, People's Republic of China*

Complete contact information is available at: https://pubs.acs.org/10.1021/acsami.2c19796

### Author Contributions

[†]Huiyong Li and Chen Shen contributed equally to this work.


### Notes

The authors declare no competing financial interest.

## ■ ACKNOWLEDGMENTS

This work was jointly supported by the National Natural Science Foundation of China (Grants 11832010, 11890682, and 21721002), the National Key Basic Research Program of China (Grant 2018YFA0208403), the Austrian−Chinese Cooperative Research and Development Projects (Project GJHZ2043), the Chinese Academy of Sciences (CAS), and the "Strategic Priority Research Program" of CAS (Grant XDB36010200).

## ■ REFERENCES

(1) Saxena, V.; Rani, R. U.; Sharma, A. K. Studies on Ultra High Solar Absorber Black Electroless Nickel Coatings on Aluminum Alloys for Space Application. *Surf. Coat. Technol.* **2006**, *201* (3−4), 855−862.

(2) Theocharous, E.; Chunnilall, C. J.; Mole, R.; Gibbs, D.; Fox, N.; Shang, N.; Howlett, G.; Jensen, B.; Taylor, R.; Reveles, J. R.; Harris, O. B.; Ahmed, N. The Partial Space Qualification of a Vertically Aligned Carbon Nanotube Coating on Aluminium Substrates for EO Applications. *Opt. Express* **2014**, *22* (6), 7290−7307.

(3) Zhou, L.; Tan, Y.; Ji, D.; Zhu, B.; Zhang, P.; Xu, J.; Gan, Q.; Yu, Z.; Zhu, J. Self-Assembly of Highly Efficient, Broadband Plasmonic Absorbers for Solar Steam Generation. *Sci. Adv.* **2016**, *2* (4), 1501227.

(4) Torres, J. F.; Tsuda, K.; Murakami, Y.; Guo, Y.; Hosseini, S.; Asselineau, C.-A.; Taheri, M.; Drewes, K.; Tricoli, A.; Lipinski, W.; Coventry, J. Highly Efficient and Durable Solar Thermal Energy Harvesting via Scalable Hierarchical Coatings Inspired by Stony Corals. *Energy Environ. Sci.* **2022**, *15* (5), 1893−1906.

(5) Wang, H.; Du, A.; Ji, X.; Zhang, C.; Zhou, B.; Zhang, Z.; Shen, J. Enhanced Photothermal Conversion by Hot-Electron Effect in Ultrablack Carbon Aerogel for Solar Steam Generation. *ACS Appl. Mater. Interfaces* **2019**, *11* (45), 42057−42065.

(6) Amemiya, K.; Koshikawa, H.; Imbe, M.; Yamaki, T.; Shitomi, H. Perfect Blackbody Sheets from Nano-Precision Microtextured Elastomers for Light and Thermal Radiation Management. *J. Mater. Chem. C* **2019**, *7* (18), 5418−5425.
(7) Moghimi, M. J.; Lin, G.; Jiang, H. Broadband and Ultrathin Infrared Stealth Sheets. *Adv. Eng. Mater.* **2018**, *20* (11), 1800038.
(8) Stavenga, D. G.; Foletti, S.; Palasantzas, G.; Arikawa, K. Light on the Moth-Eye Corneal Nipple Array of Butterflies. *Proc. Royal Soc. B* **2006**, *273* (1587), 661−667.
(9) Yang, Z.-P.; Hsieh, M.-L.; Bur, J. A.; Ci, L.; Hanssen, L. M.; Wilthan, B.; Ajayan, P. M.; Lin, S.-Y. Experimental Observation of Extremely Weak Optical Scattering from an Interlocking Carbon Nanotube Array. *Appl. Opt.* **2011**, *50* (13), 1850−1855.
(10) Kiani, F.; Sterl, F.; Tsoulos, T. V.; Weber, K.; Giessen, H.; Tagliabue, G. Ultra-Broadband and Omnidirectional Perfect Absorber Based on Copper Nanowire/Carbon Nanotube Hierarchical Structure. *ACS Photonics* **2020**, *7* (2), 366−374.
(11) Sun, P.; Zhang, W.; Zada, I.; Zhang, Y.; Gu, J.; Liu, Q.; Su, H.; Pantelic, D.; Jelenkovic, B.; Zhang, D. 3d-Structured Carbonized Sunflower Heads for Improved Energy Efficiency in Solar Steam Generation. *ACS Appl. Mater. Interfaces* **2020**, *12* (2), 2171−2179.
(12) Raut, H.; Ganesh, V.; Nair, A.; Ramakrishna, S. Anti-Reflective Coatings: A Critical, in-Depth Review. *Energy Environ. Sci.* **2011**, *4*, 3779−3804.
(13) Basheer, H. J.; Pachot, C.; Lafont, U.; Devaux, X.; Bahlawane, N. Low-Temperature Thermal Cvd of Superblack Carbon Nanotube Coatings. *Adv. Mater. Interfaces* **2017**, *4* (18), 1700238.
(14) Zhang, R. Z.; Liu, X.; Zhang, Z. M. Modeling the Optical and Radiative Properties of Vertically Aligned Carbon Nanotubes in the Infrared Region. *J. Heat Transfer* **2015**, *137* (9), 091009.
(15) Mizuno, K.; Ishii, J.; Kishida, H.; Hayamizu, Y.; Yasuda, S.; Futaba, D. N.; Yumura, M.; Hata, K. A Black Body Absorber from Vertically Aligned Single-Walled Carbon Nanotubes. *Proc. Natl. Acad. Sci. U.S.A.* **2009**, *106* (15), 6044−6047.
(16) Cheng, P.; Wang, H.; Wang, H.; Aken, P. A.; Wang, D.; Schaaf, P. High-Efficiency Photothermal Water Evaporation Using Broadband Solar Energy Harvesting by Ultrablack Silicon Structures. *Adv. Energy Sustainability Res.* **2021**, *2* (4), 2000083.
(17) Yang, J.; Luo, F.; Kao, T. S.; Li, X.; Ho, G. W.; Teng, J.; Luo, X.; Hong, M. Design and Fabrication of Broadband Ultralow Reflectivity Black Si Surfaces by Laser Micro/Nanoprocessing. *Light Sci. Appl.* **2014**, *3* (7), e185.
(18) Huang, Y.-F.; Chattopadhyay, S.; Jen, Y.-J.; Peng, C.-Y.; Liu, T.-A.; Hsu, Y.-K.; Pan, C.-L.; Lo, H.-C.; Hsu, C.-H.; Chang, Y.-H.; Lee, C.-S.; Chen, K.-H.; Chen, L.-C. Improved Broadband and Quasi-Omnidirectional Anti-Reflection Properties with Biomimetic Silicon Nanostructures. *Nat. Nanotechnol.* **2007**, *2* (12), 770−774.
(19) Liu, Z.; Liu, H.; Wang, X.; Yang, H.; Gao, J. Large Area and Broadband Ultra-Black Absorber Using Microstructured Aluminum Doped Silicon Films. *Sci. Rep.* **2017**, *7*, 42750.
(20) McCoy, D. E.; Feo, T.; Harvey, T. A.; Prum, R. O. Structural Absorption by Barbule Microstructures of Super Black Bird of Paradise Feathers. *Nat. Commun.* **2018**, *9* (1), 1.
(21) McCoy, D. E.; McCoy, V. E.; Mandsberg, N. K.; Shneidman, A. V.; Aizenberg, J.; Prum, R. O.; Haig, D. Structurally Assisted Super Black in Colourful Peacock Spiders. *Proc. Royal Soc. B* **2019**, *286* (1902), 20190589.
(22) Hu, Y.; Ma, H.; Wu, M.; Lin, T.; Yao, H.; Liu, F.; Cheng, H.; Qu, L. A Reconfigurable and Magnetically Responsive Assembly for Dynamic Solar Steam Generation. *Nat. Commun.* **2022**, *13* (1), 4335.
(23) Wang, H.; Liu, B.; Huang, W.; Lin, Z.; Luo, J.; Li, Y.; Zhuang, L.; Wang, W.; Jiang, L. Continuous Needleless Electrospinning of Magnetic Nanofibers from Magnetization-Induced Self-Assembling PVA/Ferrofluid Cone Array. *J. Magn. Magn. Mater.* **2018**, *452*, 1−4.
(24) Chen, Z.; Ye, R.; Lee, W.; Jin, D.; Zhang, Y.; Jiang, L.; Yang, Y.; Ren, L.; Jiang, L. Magnetization-Induced Self-Assembling of Bendable Microneedle Arrays for Triboelectric Nanogenerators. *Adv. Electron. Mater.* **2019**, *5* (5), 1800785.
(25) Deinega, A.; Valuev, I.; Potapkin, B.; Lozovik, Y. Minimizing Light Reflection from Dielectric Textured Surfaces. *J. Opt. Soc. Am.* **2011**, *28* (5), 770−777.
(26) Chen, H. T.; Li, C. Q.; Zhan, H.; Mo, R. W.; Zhang, Y.; Wang, J. N. Preparation of Ultrablack Composite Sheets with Excellent Mechanical and Chemical Stability from Sandpaper-Based Template-Imprinting. *Adv. Mater. Technol.* **2021**, *6* (11), 2100576.
(27) Peoples, J.; Li, X.; Lv, Y.; Qiu, J.; Huang, Z.; Ruan, X. A Strategy of Hierarchical Particle Sizes in Nanoparticle Composite for Enhancing Solar Reflection. *Int. J. Heat Mass Transfer* **2019**, *131*, 487−494.
(28) Chae, D.; Lim, H.; So, S.; Son, S.; Ju, S.; Kim, W.; Rho, J.; Lee, H. Spectrally Selective Nanoparticle Mixture Coating for Passive Daytime Radiative Cooling. *ACS Appl. Mater. Interfaces* **2021**, *13* (18), 21119−21126.
(29) Zhong, H.; Zhang, P.; Li, Y.; Yang, X.; Zhao, Y.; Wang, Z. Highly Solar-Reflective Structures for Daytime Radiative Cooling under High Humidity. *ACS Appl. Mater. Interfaces* **2020**, *12* (46), 51409−51417.
(30) Liu, Z.; Wang, H.; Huang, P.; Huang, J.; Zhang, Y.; Wang, Y.; Yu, M.; Chen, S.; Qi, D.; Wang, T.; Jiang, Y.; Chen, G.; Hu, G.; Li, W.; Yu, J.; Luo, Y.; Loh, X. J.; Liedberg, B.; Li, G.; Chen, X. Highly Stable and Stretchable Conductive Films through-Thermal-Radiation-Assisted Metal Encapsulation. *Adv. Mater.* **2019**, *31* (35), 1901360.
(31) Luo, J. C.; Gao, S. J.; Luo, H.; Wang, L.; Huang, X. W.; Guo, Z.; Lai, X. J.; Lin, L. W.; Li, R. K. Y.; Gao, J. F. Superhydrophobic and Breathable Smart Mxene-Based Textile for Multifunctional Wearable Sensing Electronics. *Chem. Eng. J.* **2021**, *406*, 126898.
(32) Yun, T. G.; Park, M.; Kim, D.-H.; Kim, D.; Cheong, J. Y.; Bae, J. G.; Han, S. M.; Kim, I.-D. All-Transparent Stretchable Electrochromic Supercapacitor Wearable Patch Device. *ACS Nano* **2019**, *13* (3), 3141−3150.
(33) Lehman, J.; Sanders, A.; Hanssen, L.; Wilthan, B.; Zeng, J.; Jensen, C. Very Black Infrared Detector from Vertically Aligned Carbon Nanotubes and Electric-Field Poling of Lithium Tantalate. *Nano Lett.* **2010**, *10* (9), 3261−3266.
(34) Hsieh, K.-C.; Tsai, T.-Y.; Wan, D.; Chen, H.-L.; Tai, N.-H. Iridescence of Patterned Carbon Nanotube Forests on Flexible Substrates: From Darkest Materials to Colorful Films. *ACS Nano* **2010**, *4* (3), 1327−1336.
(35) Yang, Z.-P.; Ci, L.; Bur, J. A.; Lin, S.-Y.; Ajayan, P. M. Experimental Observation of an Extremely Dark Material Made by a Low-Density Nanotube Array. *Nano Lett.* **2008**, *8* (2), 446−451.
(36) Sekii, Y.; Hayashi, T. Measurements of Reflectance and Thermal Emissivity of a Black Surface Created by Electrostatic Flocking with Carbon-Fiber Piles. *IEEE Trans Dielectr Electr Insul* **2009**, *16* (3), 649−654.
(37) Li, Q.; Gao, J.; Li, Z.; Yang, H.; Liu, H.; Wang, X.; Li, Y. Absorption Enhancement in Nanostructured Silicon Fabricated by Self-Assembled Nanosphere Lithography. *Opt. Mater.* **2017**, *70*, 165−170.
(38) Kanamori, Y.; Sasaki, M.; Hane, K. Broadband Antireflection Gratings Fabricated Upon Silicon Substrates. *Opt. Lett.* **1999**, *24* (20), 1422−1424.
(39) Hwang, T. Y.; Vorobyev, A. Y.; Guo, C. Formation of Solar Absorber Surface on Nickel with Femtosecond Laser Irradiation. *Appl. Phys. A: Mater. Sci. Process.* **2012**, *108* (2), 299−303.
(40) Mincuzzi, G.; Gemini, L.; Faucon, M.; Kling, R. Extending Ultra-Short Pulse Laser Texturing over Large Area. *Appl. Surf. Sci.* **2016**, *386*, 65−71.
(41) Iyengar, V. V.; Nayak, B. K.; Gupta, M. C. Ultralow Reflectance Metal Surfaces by Ultrafast Laser Texturing. *Appl. Opt.* **2010**, *49* (31), 5983−5988.
(42) Ng, C.; Yap, L. W.; Roberts, A.; Cheng, W.; Gómez, D. E. Black Gold: Broadband, High Absorption of Visible Light for Photochemical Systems. *Adv. Funct. Mater.* **2017**, *27* (2), 1604080.
(43) Ziegler, M.; Dathe, A.; Pollok, K.; Langenhorst, F.; Hübner, U.; Wang, D.; Schaaf, P. Metastable Atomic Layer Deposition: 3D Self-

Assembly toward Ultradark Materials. *ACS Nano* **2020**, *14* (11), 15023−15031.
(44) Li, Y.; Lin, C.; Wu, Z.; Chen, Z.; Chi, C.; Cao, F.; Mei, D.; Yan, H.; Tso, C. Y.; Chao, C. Y. H.; Huang, B. Solution-Processed All-Ceramic Plasmonic Metamaterials for Efficient Solar-Thermal Conversion over 100−727 °C. *Adv. Mater.* **2021**, *33* (1), 2005074.





https://doi.org/10.1021/acsami.2c19796
*ACS Appl. Mater. Interfaces* 2023, 15, 11369−11378